# Designing a VMI Spectrometer Lens for Mid Infrared Strong-Field and Attosecond XUV Photoionization Experiments

Cameron Nelson and Anthony DiChiara

Sponsored by the National Science Foundation

Undergraduate Honors Thesis

Presented in Partial Fulfillment of the Requirements for Graduation with Distinction

Ohio State University Engineering

Presented by Cameron Nelson, Engineering Physics

**Contents**

## Abstract

*A velocity map imaging spectrometer has been designed for experiments involving strong field and linear ionization of atoms using ultrashort laser pulses. The spectrometer will be used to replace conventional time-of-flight measuring devices for measuring the energy distribution of electrons released after ionization. A high energy resolution electrostatic lens design has been modeled for resolving photoelectron energies up to 400 eV and another design has been modeled for resolving photoelectrons up to 1 keV, which are a product ionization experiments involving intense, 3.6 μm wavelength laser pulses. The spectrometer is designed to be customizable, allowing for different lens designs and configurations for each experiment it is used for. The total project has been ongoing for approximately 1 year and will likely continue for another 4-6 months after the completion of this thesis.*

## Introduction

### I. Methods for Measuring Photoelectron Energy Distributions

The interaction between individual laser pulses and atoms is a widely studied field in physics and engineering. In this experimental field, lasers are used to probe and measure atomic structure and processes which would otherwise be invisible. When an electron bound to an atomic nucleus is exposed to a laser pulse, it may absorb photons if the energy $h\nu$, where h is Planck's constant ($4.136 \times 10^{-15}$ eV·s) and $\nu$ is the wavelength of the laser, from an individual photon in the laser beam is equal to the energy difference between bound states of the electron. If the energy of the photons or the intensity of the laser pulse is high enough, the electron may be ionized, where it is released in the continuum with a kinetic energy that depends on the release mechanism and properties of the laser. In some instances, the electron may even be forced back toward its atomic nucleus under the combined influence of the Coulomb force from the atomic nucleus and the laser electric field and rescatter off of the atom into the continuum. Understanding these ionization processes and the energy of the ionized electrons is a large part of current atomic physics research. Generally the ionization of individual atoms is accomplished using laser pulses with high individual photon energies ($h\nu$ greater than the ionization potential of the atom), or focused pulses with high electric field magnitudes (on the order of the binding electric field inside the atoms). In the second case, also known as strong field ionization, optically focused pulses with extremely short durations on the order of femtoseconds ($10^{-15}$ seconds) with energies on the order of millijoules are necessary for generating electric fields of this magnitude [1]. To isolate the interaction between individual atoms and laser pulses, it is necessary to focus the laser pulses into a region with low atomic density. Photoionization takes place in a volume known as the interaction region, which has a size that is dictated by the properties of the focused laser beam.

The conventional method for accurately measuring the energy of released photoelectrons from ionization interactions is to measure their time of flight over a specific distance. This gives

information about the photoelectron velocity during the flight and thus the kinetic energy. During time-of-flight measurements (TOF), electric fields can be used to slow down or accelerate electron flight paths. Although the TOF method is widely used and creates accurate results, TOF spectrometers generally have one significant disadvantage: the photoelectron energy distribution from ionization interactions is two-dimensional, assuming a symmetry axis along the polarization direction of the laser, and TOF spectrometers are designed to measure the energy distribution only along one dimension. The importance of measuring in two dimensions is especially true when the ionization event involves photoelectron rescattering, where the photoelectron has a larger probability of being released into the continuum at a significant angle. To compensate for its lack of visibility, a TOF spectrometer needs to be rotated around the interaction region to resolve the entire ionization interaction. TOF spectrometers used in strong field experiments have measuring angles of approximately 2 degrees and an individual TOF measurement of the interaction region usually take several minutes, so imaging the entire interaction region may take several hours. An alternative to TOF spectroscopy is velocity map imaging (VMI) spectroscopy [1,6], where the 3-D energy distribution of photoelectrons is projected and mapped onto a 2-D plane, thus resolving the entire released photoelectron distribution at once. As a result, information about the interaction region is gained in a much shorter time frame, which saves valuable lab time.

## II. Physical Descriptions of Photoionization Experiments

There are essentially two classes of experiments that will feature the VMI spectrometer designs presented in this text. Both experiments use ultrashort laser pulses, which have durations from 150 femtoseconds ($10^{-15}$ seconds) to hundreds of attoseconds ($10^{-18}$ seconds), to ionize atoms. Creating pulses with femtosecond durations has been a technological possibility since the 1980s [3], and it is now possible to create them using a commercial setup that can fit on a laboratory tabletop. Attosecond science is still a relatively new field which requires more sophisticated techniques for creating pulses. Generally, experiments featuring photoionization with femtosecond lasers use very high intensity pulses ($>10^{14}$ Watts/cm$^2$) with long laser wavelengths (from 0.8-3.6 μm). Attosecond laser experiments use low intensity pulses with short laser wavelengths (XUV or soft X-ray). The optical period of a laser depends on its central wavelength, but is usually ~1-10 femtoseconds for most laser experiments. Attosecond lasers have pulse durations that are a fraction of this optical period, so pulses with short laser wavelengths therefore must be used to create these pulses. Because of the different laser characteristics in each ultrashort photoionization experiment, the photoionization dynamics are also expectedly different. This section will highlight some of the physical mechanisms involved in ionization from femtosecond and attosecond pulses (parts b and c) and the methods of creating ultrashort pulses (part a). A short discussion of the types of energies in strong field interactions will conclude this section in part d.

### a.) Creating Ultrashort Laser Pulses

Laser pulses with femtosecond and attosecond durations are generated with different techniques that rely roughly on the same general concept, laser modelocking [3]. A laser cavity can support an infinite number of standing light wave modes that are separated in frequency by the free spectral range of the laser $\Delta\nu_{fsr} = c/2L$, where L is the length of the laser cavity and c is the speed of light. The laser gain media has a specific bandwidth in frequency space at which it will lase, therefore the number of cavity modes that the laser has access to is limited by this bandwidth. If a laser is modelocked, each cavity mode that it has access to will be locked in phase and can each interfere such that a single, short-duration pulse is created. Pulses will emerge from the laser output coupler at a repetition rate given by $f_{rep} = c/2L$. The duration of the laser pulse is governed by how many laser modes may interfere to create it, and is proportional to 1/N, where N is the number of modes. The bandwidth of the laser gain medium therefore determines the pulse duration of a modelocked laser, since it dictates the number of modes a laser cavity may lase with. Creating femtosecond pulses is possible with gain media like Titanium:Sapphire (Ti:Saph), which has a frequency bandwidth of ~128 THz. Creating pulses that have durations ~100 attoseconds requires a bandwidth of ~5 x $10^3$ THz, or ~40 eV if scaled by Planck's constant, which cannot be achieved using known laser gain media materials. One method for attaining this level of bandwidth lies in the utilization of signals obtained from high harmonic generation in a gas [2]. If an intense laser beam is focused into a gas with sufficient density, photons with high energies may be created as a result of the ionization and recombination of electrons. Photons are emitted with frequencies that are odd multiples of the fundamental laser frequency, so a laser with frequency $\nu$ may generate a frequencies $q\nu$, where q is an odd number [2]. In frequency space, emission from high harmonic generation can be represented as a comb, with separation between the "teeth" given by q [3]. High harmonic generation has the capability of providing the bandwidth for pulses with durations ~100 attoseconds. An example high harmonic frequency spectrum is shown in fig. 1 below.

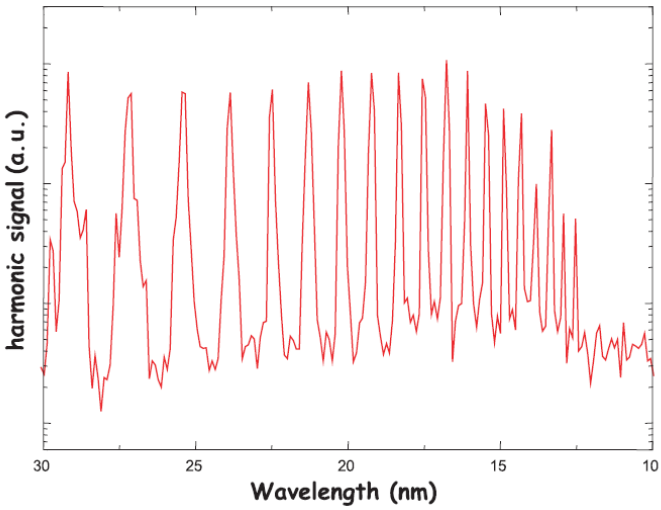


Figure 1: Frequency representation of high harmonic generation in neon gas. In this experiment, 50 ns, 800 nm pulses irradiated a sample of neon, resulting in a high harmonic spectrum output. Figure taken from [3].

It is also possible to lock the phases of the harmonics emitted from the gas, so high harmonic generation can be used as a substitute for modelocking [3]. In this way, pulses with attosecond

duration may be created from interference of the output light in a high harmonic generation experiment.

### b.) Linear and Non-Linear Photoionization

Electrons are bound to their parent atoms by the Coulomb potential, which scales like *1/r*, where *r* is the separation distance between the atom and its nucleus. By convention, electrons in bound states have negative potential energies and are promoted to more excited states when given a positive increase in energy. Because of quantum mechanics, the energy separation of each bound state is quantized, so an electron must absorb a photon with energy $h\nu$ equal to this separation. If the energy of the photon is stronger than the atomic binding potential $I_0$, the electron will be promoted to the continuum with a residual kinetic energy given by eqn 1, which is a variant of the photoelectric effect.

$$E = h\nu - I_0 \tag{1}$$

If a single photon is absorbed by an atom and an electron bound to the atom is promoted to the continuum, the photoionization is linear. If the laser wavelength is too low to ionize the electron, ionization processes are more complicated, because additional photoelectrons are required to overcome the ionization potential. Non-linear or multiphoton ionization occurs when photoelectrons are promoted to excited bound levels and subsequently ionized by absorbing additional photons at these levels. This requires a much more intense laser pulse than in linear ionization interactions [4]. The non-linear photoelectron energy is obtained by multiplying hν in eqn 1 by n, the number of photons required to promote the bound electron into the continuum.

As was mentioned previously, attosecond pulses are usually created with relatively low intensities. Because of the low intensity and high frequency components of attosecond pulses, the photoionization processes using these pulses is generally linear. Figure 1 gives a good representation of a sample photon energy range an attosecond pulse may carry. Each part of the frequency comb is separated by 3.1 eV [3], with a highest energy in the comb of 94.6 eV. Table 1 shows the ionization potentials of 3 noble gases that are typically used in photoionization experiments. The released photoelectron energy range from attosecond experiments can therefore be obtained from frequency spectra like fig. 1 by subtracting the ionization potentials from table 1 from the energy of the comb components. Typically, the photoelectron energy range does not exceed 100 eV.

| Element | Ionization Potential (eV) |
|---|---|
| Neon | 21.56 |
| Xenon | 12.13 |
| Argon | 15.76 |

Table 1

### c.) Strong-Field Photoionization

If the intensity of the laser pulse is increased further beyond the realm of multiphoton photoionization, the pulse can be treated as a classically oscillating electric field, with amplitude given by eqn 2, which is time-varying due to the shape of the pulse envelope [4].

$$E_{Laser} = E_0(t)\sin(\omega t) \tag{2}$$

A free electron in this laser field will have a velocity as a function of time that can be determined using Newton's second law and the force $F = qE_{Laser}$. The cycle averaged kinetic energy of this oscillating electron is called the ponderomotive potential $U_p$, and is given by eqn 3.

$$U_P = \langle \frac{1}{2} m {v_{electron}}^2 \rangle = \frac{e^2 {E_0}^2}{4m\omega^2} \tag{3}$$

As an intense laser pulse interacts with a bound electron, the excited states, except for the few lowest excited states, of the electron/atom system shift downward in energy by an amount equal to $U_p$ [4]. Physically this is because the laser must provide enough energy to ionize the photoelectron and start its motion in the laser field. As the laser pulse electric field decreases in amplitude, the excited states of the bound electron/atom system also shift upward again. The intensity and wavelength of the laser can be adjusted such that the shifts in the excited state energies given by the ponderomotive potential will be equal to multiples of the photon energy. When this happens, the excited states of the electron will pass through transient resonances, where it is likely that the electron will absorb additional photons. Because the excited states shift into transient resonances during the laser pulse, the electron may absorb more photons than needed for multi-photon ionization, which changes the energy gained from ionization [4]. This type of ionization is known as above threshold ionization (ATI) [4], and the energies of photoelectrons released in these interactions is given by eqn 4 [4].

$$E = (n+s)h\nu - I_0(I) - U_p(I) \tag{4}$$

In equation 4, *s* represents the excess number of electrons absorbed above what is needed for photoionization, and it is explicitly shown that that binding potential and ponderomotive potential become functions of the laser intensity *I*.

As the intensity of the laser is increased further beyond the intensity levels in the realm of ATI, the electric potential of the laser becomes strong enough to bend the Coulomb barrier of the atom. Depending on the wavelength of the laser, the ponderomotive shift of the atomic energy levels may be so high that the role of individual photons in the ionization process is no longer important, and ionization dynamics take a different form. Equation 5 gives a more precise description of the effect the laser field has on the Coulomb potential, where it is assumed that the laser field and Coulomb potential are centered in the direction of y.

$$U_{eff} = U_{atom} + U_{Laser} = -\frac{1}{4\pi\epsilon_0}\frac{Ze}{y} - E(t)y \tag{5}$$

Shown in fig. 2 is the effect of the laser field on the Coulomb potential. The solid line in fig. 2 shows the combined potential energy of the laser and atom, which results in a bent form of the atom Coulomb potential. The left vertical axis gives the potential energy in units of an arbitrary bound state $E_{IP}$, where negative energy values indicate that this state is bound to the atom. If the intensity of the laser pulse is strong enough, the Coulomb barrier may be bent enough such that the $E_{IP}$ level is completely exposed. For a given laser wavelength, the intensity at which this

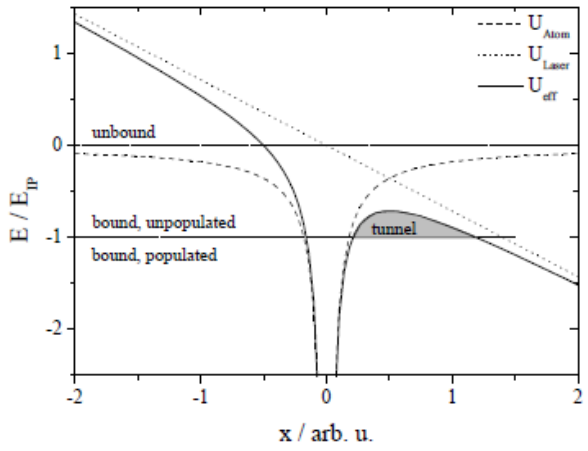


Figure 2: Coulomb potential (dot-dashed line) subtracted from laser potential (dotted line) and plotted as bent Coulomb potential (solid line) for an arbitrary atom. The energy scale (vertical axis) is in units of an arbitrary bound state $E_{IP}$. Figure taken from [1].

occurs is called the saturation intensity, since electrons bounded by the atom will ionize with a very high probability.

An effect of quantum mechanics is tunneling, where an electron wave packet has a finite probability of tunneling through a potential energy barrier. If the Coulomb barrier is suppressed sufficiently, an electron may tunnel into the continuum with a high likelihood. A good measurement for the likelihood of tunneling through the Coulomb barrier is given by the Keldysh parameter γ in equation 4, where T is the period of the laser electric field [4].

$$\gamma = 2\pi \frac{t_{tunnel}}{T} \tag{6}$$

If the Keldysh parameter is $\ll 1$, ionization by tunneling is likely. As the laser frequency decreases and the period increases, the Coulomb potential is suppressed for a longer period of time, thus tunneling becomes more and more likely as the photoelectron has more chances to pass through the depressed Coulomb barrier. The motions of bound electrons within atoms typically takes place on a time scale of ~25 attoseconds [1], so the wavelength of the laser pulse should be long enough such that the Coulomb barrier is suppressed for a much larger period than the electron motion timescale.

### d.) Photoelectron Energy Distributions from Strong-Field Photoionization

Unlike the example of linear ionization with attosecond pulses, the photoelectron energy distribution from strong field photoionization does not depend strictly on the wavelength of the laser used. The ionization process also depends on the pulse duration, since the Keldysh parameter will become higher as the duration becomes shorter. The intensity of the laser pulse also plays an important role in determining the photoelectron distribution. Immediately after a photoelectron tunnels out of the Coulomb barrier, it essentially has no kinetic energy. At this point, the electron is strongly under the influence of the electric field of the laser. If the photoelectron moves away from the interaction region before the laser field changes direction, it will move into the continuum with a kinetic energy determined by the laser intensity and wavelength. Because the electron's motion is determined by how much energy it can gain by the oscillating electric field, the energy a photoelectron may gain from the field is proportional to its ponderomotive potential. The photoelectron can gain a maximum kinetic energy of $3.17U_p$ from the laser field, or up to $10U_p$ if it rescatters elastically from the atomic nucleus into the continuum [4]. The ponderomotive potential is inversely proportional to the square of the frequency of the laser for a fixed intensity, so longer wavelength lasers are expected to give higher photoelectron energy distributions overall. Figure 3 shows a graph from a strong field experiment involving the photoionization of argon atoms in 2008 [8]. This figure also illustrates the range of laser wavelengths that will be used in experiments featuring the VMI. The intensity of the lasers used in the experiment was .08 petawatts/cm$^2$ (1 petawatt = $10^{15}$ watts). Generally, the laser intensities do not vary over a large range in strong field experiments, although slight variations in intensity may be used depending on the ionization potential of the atom studied. From fig. 3, the actual photoelectron energies can be estimated based on the laser wavelength used. It can be seen that most long-wavelength photoelectrons have energy in a range between 0-300 eV, however rescattered photoelectrons from 3.6 μm lasers may have energies up to 1 keV.

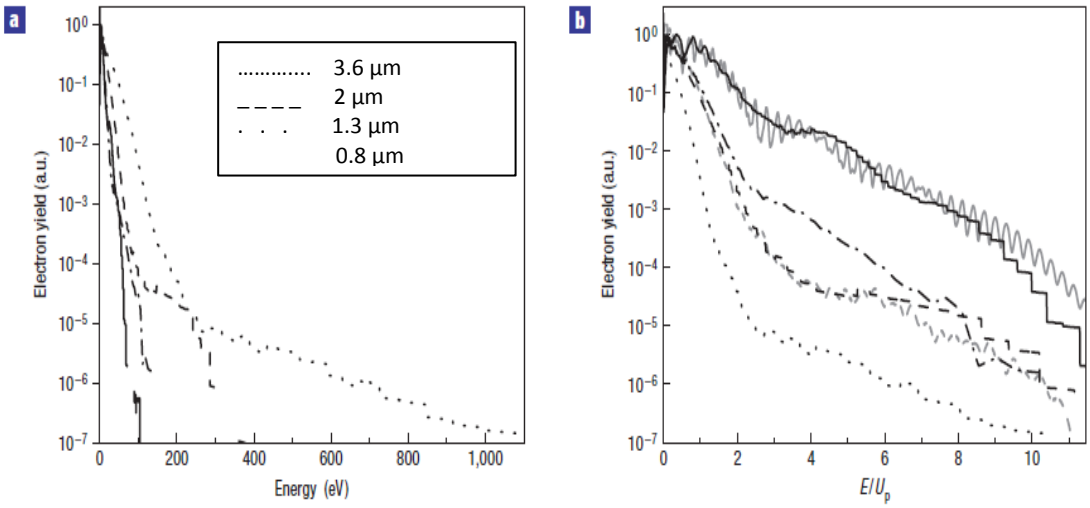

Figure 3: a.) Plot of photoelectron yield as a function of photoelectron initial energy for various wavelengths in a strong field experiment featuring a .08 PW/cm$^2$ intensity laser in the interrogation of argon. b.) Plot of photoelectron energy as a function of the ponderomotive potential of the electron. Solid squiggly line is a time-dependent Schrodinger equation model for the energy distribution. Figure taken from [8].

## Overview of the VMI Spectrometer

### I. Introduction to the VMI Components and their Functions

Essentially the VMI spectrometer consists of two crucial parts: an electrostatic lens and a photoelectron detector. *The photoelectron detector properties will be discussed briefly in this thesis, but the main focus will be the modeling of the electrostatic lens component. The detector component is typically not designed in the VMI model, and is made to order by a photonics company. The most physics-related work in this projected was centered on the VMI lens construction; therefore it is fitting that the thesis discuss this process in detail.* The photoionization interaction region is located between two of the lens components and the resulting photoelectron or photoion distribution is pushed by the lens onto the detector. The VMI electrostatic lens bends the photofragment trajectories such that photofragments with the same initial momentum vector are focused onto the same physical point on the detector face. The voltage sign of the lens components determines the type of photofragment it focuses. If the lens plates are charged to a positive voltage, the lens will focus photoions, and vice versa for photoelectrons. The electrostatic lens performance in conjunction with the detector depends on the initial energies of the photoelectrons. The VMI design featured in this text will be customizable for two different photoionization experiments with drastically different photoelectron energies; therefore two different lens designs were modeled.

An Autodesk Inventor drawing of the VMI assembly is shown in fig 4. All of the VMI components are kept in a vacuum chamber to improve the performance of the detector and to avoid collisions between the released photoelectrons and stray molecules. The entire VMI assembly is mounted on an 8'' zero-length reducer flange which will be vertically inserted into a 6-way cross vacuum chamber. The photoelectron detector (metallic object in fig. 4) is mounted onto a copper stand which is attached to the zero-length reducer. Using alumina-oxide spacers, the detector can be moved closer to the interaction region if needed. The lens assembly is designed such that the interaction region is exactly in the center of the vacuum chamber. A focused laser beam will pass through one of the chamber crosses, intersecting the interaction region. An effusive backfill system will flood the vacuum chamber with the target gas used in the experiment while keeping the chamber at an acceptable vacuum level, $10^{-5}$ torr.

Most of the following section will discuss properties of the VMI electrostatic lens, with a very short section on the operation of the photoelectron detector. Particular emphasis will be put on the focusing properties of the lens and how the interaction region is formed onto the detector face. Additionally, the inverse Abel-transform method for recreating the full 3-D initial momentum distribution of photoelectrons and computer modeling methods of the lens will be mentioned.

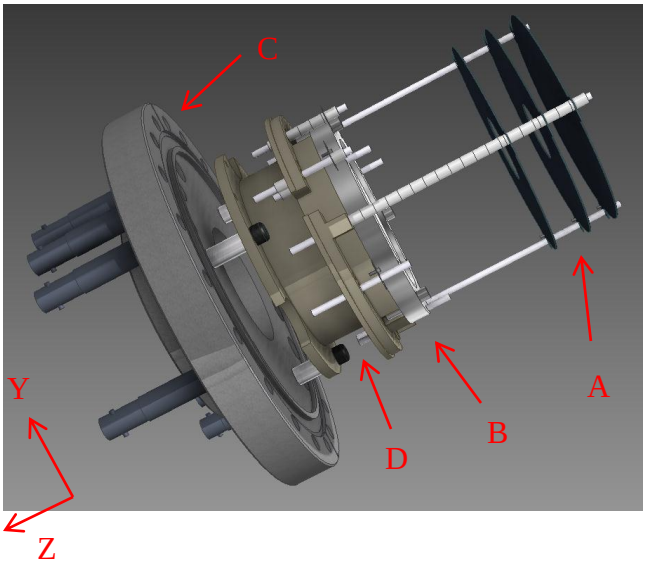


Figure 4: AutoDesk Inventor 3-D Rendering of VMI Assembly. The lens component (A) rests on alumina-oxide spacers. The interaction region is created between the two right lens plates. The detector (B) is bolted to a copper stand (D). The detector position with respect to the lens can be adjusted using additional spacers. The entire assembly is mounted onto an 8'' zero-length reducer flange (D).

## II. The VMI Electrostatic Lens

The electrostatic lens is essentially the most user-controlled and customizable part of the VMI. The lens focusing properties can be controlled and changed by altering the size and geometry of the lens components or by applying different voltages to the lens plates. The lens focuses photoelectrons based on their initial momenta, so the design of the lens must be dependent on the photoelectron energies it is intended to resolve. The electrostatic lens is made from three electrodes charged by DC electric fields which are designed to push photoelectrons away from the interaction region. The three electrodes are differentially charged, creating an asymmetric immersion lens. In an asymmetric immersion lens, the repeller plate, located on the far right in fig. 4 is held at a higher voltage magnitude than the extractor plate, located in the middle of the plate assembly in fig. 4. The plate on the left of the lens assembly is grounded to prevent further lens focusing outside of the assembly and to establish a large potential gradient between it and the extractor. This design is important for photoelectron focusing, which will also be discussed in detail during this chapter. The interaction region is generally located between the extractor and repeller plate in the center of the plate apertures, but its position can be adjusted based on the lens operation.

### a.) Imaging and Focusing the Interaction Region with an Electrostatic Lens

During photoionization, electrons are essentially ionized along the polarization direction of a focused laser pulse within a finite volume. In momentum space, the photoelectrons can be mapped onto cones with apexes along the polarization of the laser, as shown in fig. 5a. The purpose of the electrostatic lens component in the VMI is to project these cones onto a flat 2-D surface and recreate the 3-D initial momentum distribution using an inverse-Abel, or back-projection technique. In this process, the angle $\phi$ in fig. 5a is conserved, thus the 2-D projection will resemble a slice through the momentum distribution in the $P_x$-$P_y$ plane.

In classical optics, an optical lens is used to bend rays of light to a convergent location known as the focus. In a similar way, an electrostatic lens is used to bend charged particle paths to a specific spatial focus. The focusing properties of an optical lens depend on its shape and relative indices of refraction. As an electrostatic lens is charged, lines in space surrounding the lens trace out equipotentials, or imaginary lines of equal electrical potential, shown in a 2-D lens cross-section in fig. 5b. The shape of these lines and the differences in electrical potential between the lines determine the lens focusing properties. In this way, the electric potentials in an electrostatic lens are analogous to the indices of refraction in an optical lens. The focusing properties of an electrostatic lens differ greatly from and optical lens however. Unlike light rays, which have the same speed in a medium with a constant index of refraction, charged particles released from the interaction region in general do not have the same velocity. Only charged particles with the same initial velocity vector (magnitude and direction) will be focused to the same point at the focal plane of an electrostatic lens.

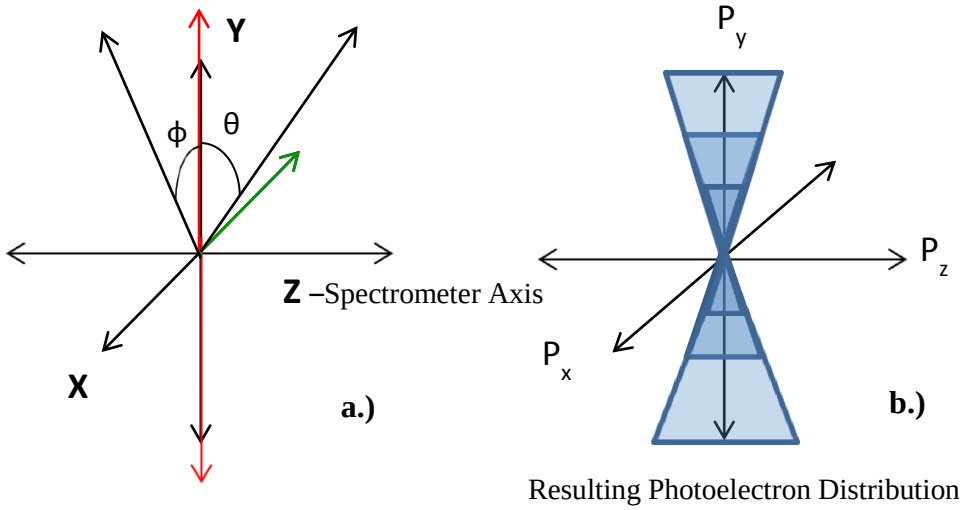


Figure 5: a.): Coordinate system for VMI interaction region. The red arrow is the polarization direction of the laser and the green arrow is the propagation direction. b.): Shape of photoelectron distribution from photoionization interaction in momentum space.

Consider a 3-D distribution of electrons in space within a finite volume that has an isotropic momentum distribution at birth (the same density of initial velocity vectors in all directions). In momentum space, electrons in this distribution can be mapped on concentric spheres with radii determined by the velocity magnitude of the electrons. If the same 3-D cloud of electrons is concentrated to a single point in real space, the electrons in real space will be found on the same spheres that make up the initial momentum distribution after a sufficient amount of time has elapsed. If this concentrated photoelectron distribution is projected onto a 2-D detector surface in space, the detector will pick up a 2-D photoelectron pattern that resembles a cut in the 3-D momentum distribution in the $P_x$-$P_y$ plane. In other words, the detector will see rings of photoelectrons that resemble the 2-D cross section of the 3-D momentum distribution. In a VMI, the interaction region is not literally focused to a point, but the focusing properties of the lens map photoelectrons with the same initial velocity vector onto the same point at a 2-D plane,

which has the same effect. To sum up, photoelectrons with the same initial velocity vector but different spatial orientation in the interaction region converge more or less to the same point at the lens focal plane if the lens is in focus. Effective space focusing requires constricting the interaction region along the spectrometer axis (Z direction in fig. 5a) and independently along the X and Y axes in fig 5. Because of cylindrical symmetry around the Z direction, the focusing effect of the lens in X and Y is equivalent.

One effect of the 3-D initial momentum distribution projection caused by the VMI electrostatic lens is that photoelectrons launched along the polarization direction of the laser will form concentrated rings on the 2-D detector surface. This effect can be visualized in two ways. First, the detector image in a focused VMI is a representation of a 2-D slice in the $P_x$-$P_y$ plane of the initial momentum distribution. Since this initial momentum distribution is composed of concentric spherical distributions with radii dependent photoelectron energies, the detector surface should resemble a cut through these spheres, or circles, shown with real data in fig. 6a. Figure 6b shows another way of visualizing this effect in the Simion 7.0 interface which relies on the fact that photoelectrons with different launch elevation angles θ (see fig. 5) are focused to different points on the detector. As shown in fig. 5b, photoelectrons launched with small angles θ will generally converge to a more concentrated location on the detector surface. The VMI lens does not distinguish photoelectrons with the same angle θ, so photoelectrons launched along –θ directions are equivalently focused.

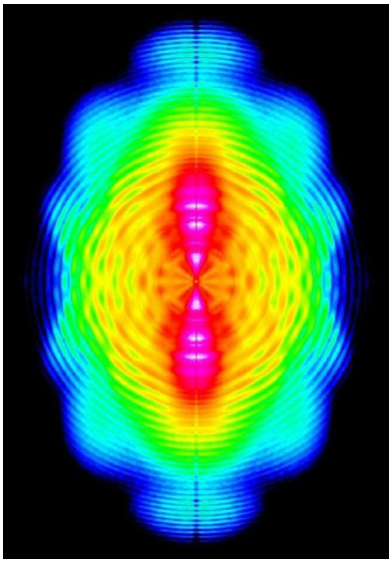

a.)

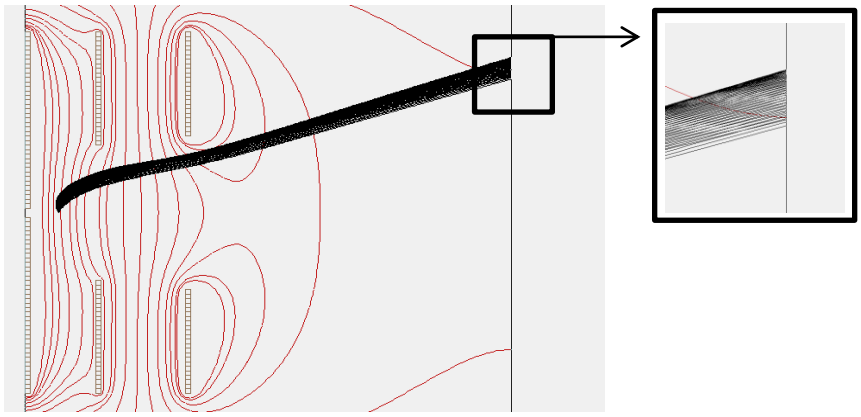

b.)

Figure 6: a.) 2-D detector image with actual VMI data from [1]. Photoelectrons launched with $\theta = 0$ form concentric rings on the image which are used as an initial condition for the reverse-Abel transform program. b.) Simion 7.0 interface showing a cross-section of an electrostatic lens design. A group of 60 photoelectron trajectories was launched with varying angles $\theta$. Photoelectrons with low $\theta$ launch angles form tight bunches at the detector plane (top of photoelectron bunch in zoomed in picture). Equipotential lines are drawn in red.

The inverse-Abel Transform method [9] for recreating the initial 3-D momentum distribution of the photoelectrons depends on the fact the focusing effect of photoelectrons launched with an angle $\theta$ is not dependent on the sign of $\theta$. In other words, the photoelectron distribution is cylindrically symmetric around the polarization direction of the laser Y. Because of this fact, the 3-D initial momentum distribution can be recreated with disks along the $P_y$ axis with thickness $dP_y$. The photoelectron distribution is in each disk conserved along the rotation of the $P_y$ axis and determined along the $P_x$ axis by the photoelectron ring concentration along the X direction of the detector image. Because the detector rings spacings are essentially determined by the photoelectron energies, the expected radii of the initial 3-D photoelectron momentum distribution can also be predicted. The relative photoelectron concentrations in the detector rings and the expected radii of the 3-D disks can be used to guess a 3-D initial momentum distribution. This guess can be simulated and tested against the detector signal until convergence is reached. In this way, an iterative computer algorithm can be used to recreate the initial 3-D photoelectron momentum distribution from information provided by the detector signal [10].

The VMI lens focuses separately along the spectrometer axis (Z) and the propagation and polarization axes (X and Y). The VMI lens is more or less in-focus along the spectrometer axis if parts of the interaction region have equivalent or less equivalent times of flight to the detector. This can be accomplished by increasing the voltage magnitudes of the extractor and repeller plates. Increasing the voltage magnitude of the entire lens has the effect of increasing voltage gradients between the plates, which results in a stronger pushing force on the interaction region. For a fixed lens voltage magnitude, adjusting the voltage ratio $X_v = V_{Extractor}/V_{Repeller}$ or the length of the field-free region also has an effect on the lens focusing along the spectrometer axis. This is the first way in which the lens acts to constrict the apparent size of the interaction region. In an ideally Z-focused lens, the effective shape of the interaction region would be a completely flattened disk, where the spatial area is restricted to the X and Y directions only. Focusing the VMI lens in the X-Y directions shown in fig. 5 is accomplished by changing $X_v$ only. By changing the lens bias ratio, equipotential lines between the lens plates become more or less constricted, facilitating the focus of photoelectrons with a specific energy. The focusing effect of the lens in all three spatial directions is therefore dependent on the initial velocities of the photoelectrons. By adjusting the bias ratio $X_v$ for a fixed voltage magnitude applied to the repeller, photoelectrons with different energies converge more or less to the same point at the lens focal plane. Using the isotropic momentum distribution example given above, this is equivalent to bringing concentric spheres in momentum space more or less into focus as they are projected onto the detector.

### b.) Computer Modeling of the VMI Electrostatic Lens

Modeling the electrostatic lens components of the VMI can be accomplished using the computer program Simion 7.0. In Simion, a user can create models of biased electrodes and "flies" photoelectrons with designated positions, initial energies and release angles. The electrodes are placed in a 3-D grid with millimeter point separation. After photoelectrons trajectories are calculated, selected output data may be taken from Simion, including information about final kinetic energies of the photoelectrons, positions of the photoelectrons as they strike the boundaries of the grid and time of flight information. Another useful feature of Simion is the capability of plotting equipotential lines and equipotential gradients within the grid. A screenshot of the Simion interface is shown in figure 6b. along with plotted equipotential lines and photoelectron trajectories.

## III. The VMI Detector

The VMI uses a microchannel plate (MCP) detector to capture photoelectrons from the interaction region. The front face of the microchannel plate is bored with equally spaced pores that are ~10 μm in diameter. Each bored hole is an electron multiplier, so the output side of the detector outputs an electric signal that retains position information of the photoelectron that strikes the screen. A phosphor screen is placed behind the MCP detector to capture the electric signal from the microchannels. An example signal from a phosphor screen is shown in fig. 6a. As the phosphor screen illuminates, a CCD camera captures the resulting illumination, which relays this data to a computer for storage. The stored data is used in the iterative inverse-Abel transformation.

### Designing a VMI Electrostatic Lens for Strong Field Experiments

As mentioned in previous sections, the focusing effect of the VMI electrostatic lens depends on the energy of the photoelectrons being focused. Each photoelectron energy is separately focused in the X and Y direction depending on the value of $X_v$, however the Z focusing of photoelectrons is ideally not energy dependent. Focusing the photoelectron paths onto the detector requires bending photoelectrons that have initial momenta strongly centered along the Y axis. Photoelectrons with higher energies require more bending, so the strength of the lens (voltage magnitude) also needs to be tailored to the photoelectron energy distribution one is interested in measuring. Finally, the diameter of the detector with respect to the photoelectron energy plays an important role in the lens design. Photoelectrons with higher energies and lower angles θ are focused to a larger radius on the detector (in the X-Y plane), so the photoelectron trajectories may require additional bending if they are focused to a position greater than the detector diameter. All of these factors must be strongly considered when designing a lens for strong field interactions at long wavelengths, with relatively high photoelectron energies.

The first VMI spectrometer design was published in 1997 by Eppink and Parker [6]. It was designed for a photodissociation experiment involving molecular oxygen, and was used to measure the initial velocity distributions of the resulting $O_2$ ions. Photoions in this experiment had initial energies between 1-4 eV, and the electrostatic lens was designed for the best resolution around this energy. A second design by Matthias Kuebel [1], modified the design from Eppink and Parker to include photoelectrons with initial energies up to 80 eV. Additional designs and modifications to VMI electrostatic lenses have also been published [5], but none have considered lens designs capable of resolving photofragments with energies higher than 80 eV. Ultimately the photoelectron energy a VMI electrostatic lens may resolve is limited by the maximum lens voltage and detector diameter. Eppink and Parker used a 1 kV power supply to charge their lens plates and Matthias Kuebel used a 10 kV supply in his design. Both of these VMI examples used a 40 mm diameter detector. To resolve photoelectrons with energies up to 1 keV with this detector size, either a very high voltage power supply (20 kV or greater) must be used, or significant modifications need to be applied to the previous designs. In August 2010, it was decided to design an electrostatic lens using a 10 kV power supply and a 75 mm detector to resolve up 1 keV photoelectrons produced in strong field experiments. It was also decided that a good initial stepping stone in achieving this goal was to design a lens capable of resolving up to 400 eV photoelectrons with the same power supply and detector diameter. The 400 eV lens design will be used primarily in lower wavelength strong field experiments and attosecond photoionization experiments, therefore its performance will be geared toward photoelectron energies from 0-200 eV.

Using Matthias Kuebel's design as a starting point for the 400 eV design, we immediately noticed a problem in the lens performance with 400 eV photoelectrons launched along the laser polarization direction. With a 10 kV applied voltage ($V_R$ = -10 kV), the photoelectrons clipped the lens plate components on their way to the detector due to their large initial velocity in the Y direction. Changing the focusing properties of the lens by altering $X_v$ did not allow the photoelectrons to pass through the apertures. The first necessary step in the design procedure therefore was to expand the apertures of the lens, in particular the aperture of the ground plate as it most directly affected the photoelectron clipping. Because of detector diameter limitations and the large initial velocity of photoelectrons released along the laser polarization direction, it was necessary to move the focal plane inward toward the repeller (-Z direction). To compare, the field-free region in Matthias Keubel's final design was 126 mm and was changed to 73 mm after necessary modifications. Qualitatively, the effect of moving the focal plane inward generally leads to decreased lens resolution $\Delta E/E$. This is because groups of focused photoelectron trajectories have less time to spread out spatially before they cross the lens focal plane. With these two design modifications in place, it was then possible to begin maximizing the lens resolution and performance.

## I. Gaussian Beam Optics and the Constriction of the Interaction Region

The resolving capability of the VMI is highly affected by the size of the interaction region volume. As the interaction region size increases, the focusing effect of the lens needs to be greater to collapse this region to an apparent point in space. The first step in maximizing the lens performance should therefore involve the determination of the interaction region size.

Laser pulses are focused to the interaction region using an optical lens. The intensity profile at the laser focus can be approximated using Gaussian optics [7], where the intensity as a function of position is given by eqn. 6. In eqn. 6, w[X] represents the size of the beam around the propagation direction as a function of distance along the propagation direction. The parameter w0 represents the minimum spot size and r = $\sqrt{Z^2 + Y^2}$, the radial distance from the axis of propagation.

$$I(r, X) = I_0[\frac{w_0}{w(X)}]^2 \exp[\frac{-2r^2}{w^2(X)}] \tag{6}$$

The minimum spot size w0 is directly proportional to the wavelength of the laser and the f number (f/#) of the optical lens used to focus the pulses, which is defined as the ratio of the lens focal length to the physical diameter of the lens. The spot size w[X] is given by eqn 7 in terms of the minimum beam waist. The parameter $x_{R,}$ defined in eqn 8, is known as the Raleigh length [7] and gives the location along the propagation axis of the FWHM of the intensity profile. The dependence of w[X] on the minimum spot size implies that the Gaussian intensity profile becomes more constricted as the f number of the lens is decreased. A graphical representation of the 2-D intensity profile at a Gaussian beam focus is shown in figure 7.

$$w[X] = w_0\sqrt{1 + (\frac{X}{X_R})^2} \tag{7}$$

$$X_R = \frac{\pi {w_0}^2}{\lambda} \tag{8}$$

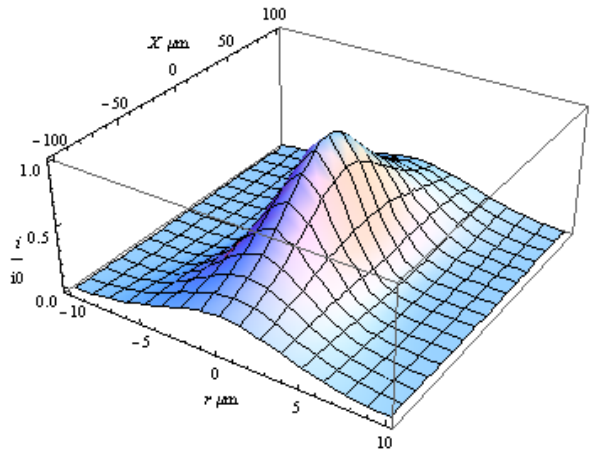


Figure 7: Normalized 3-D plot of intensity vs 2-D position at a Gaussian laser focus for an f/# = 4 lens.

If the central intensity of the laser in the interaction region is $I_0$, the photoelectron yield drops roughly like $I^8$ away from the central intensity [8]. That is, if the photoelectron yield at the

central intensity of the focus is $P_0$ and the intensity drops to $I_0/5$, the photoelectron yield will drop to $P_0$ x $.2^8$ or $2.56P_0$ x $10^{-6}$. To constrict the size of the interaction region, the point along X where the central intensity drops by a factor of 5 was used as a spatial cutoff. For an f/# = 4 lens, the interaction region length (or size along the X direction) and spot size (minimum beam waist) is given as a function of frequency by table 2.

| Laser Wavelength (μm) | Interaction Region Length (mm) | Minimum Beam Waist (μm) |
|---|---|---|
| 0.8 | 0.2316 | 3.84 |
| 1.2 | 0.3474 | 5.76 |
| 2.0 | 0.5791 | 9.60 |
| 3.6 | 1.0423 | 17.28 |

Table 2: Size of the interaction region for various laser wavlengths for an f/# = 4 optical lens

As the f/# of the lens is decreased, the beam divergence angle, given by eqn 9, with λ equal to the wavelength of the laser, $w_0$ the minimum beam waist and X >> $X_R$, becomes greater.

$$\theta_D = \frac{\lambda}{\pi w_0} \tag{9}$$

The laser pulses are focused into a vacuum chamber between the extractor and repeller plates to meet the potentially ionized atoms at the interaction region. It is usually impractical to insert an optical focusing lens into the vacuum chamber, so the lens will look into the chamber from a window attachment. This set-up will eventually limit the size of the lens f/#, since the focused pulses will eventually clip the lens components as the beam divergence angle increases. We determined that an f/# = 4 lens is the roughly the smallest possible f/# to use in our experiment to avoid clipping the lens components due to the high divergence angle of this lens, therefore the remainder of the design was constructed with an f/# = 4 lens in mind.

## II. Maximizing Lens Resolution and Performance

Choosing an f/# = 4 lens effectively limits the position of the interaction region along the spectrometer axis. For a given lens geometry and photoelectron energy, a necessary first step in testing the lens performance is to make sure photoelectrons can possibly pass through the lens apertures and converge on the detector. This method was discussed previously and applied to the lens design in [1] to give a starting lens template for resolution optimization.

The spectrometer function of the VMI determines the maximum radial distance on the detector a photoelectron of a given energy will be found, which translates to mapping the radial detector positions of photoelectrons launched along the polarization direction of the laser. In other VMI designs [1, 6], it has been found that the spectrometer function r when plotted as a

function of the photoelectron energy $E^{1/2}$ is very nearly linear. As a result of this linearity, the energy resolution for particular photoelectron energies can be found. Photoelectron groups with the same energy form rings on the detector with radii r and radial thicknesses Δr that depend on the focusing properties of the lens. If the spectrometer function can be written in the form of equation 10, the resolution of the lens can be determined by equation 11, which obtained from the differential Δr/ΔE of the spectrometer function.

$$r = kE^{1/2} \tag{10}$$

$$\frac{\Delta r}{r} = \frac{1}{2}\frac{\Delta E}{E} \tag{11}$$

Equation 11 essentially allows for a measure of the lens resolution as a function of the spot size and detector position for a particular photoelectron group, information that can be obtained from simulation.

As was mentioned previously, a properly focused electrostatic lens in the VMI assembly effectively collapses the interaction region in two independent directions, Z and Y (focusing in Y is equivalent to focusing in X). Normally focusing along the Z axis is accomplished by changing the voltage magnitude of the lens components to create larger electric potential gradients. As was discussed in a previous section, the 400 eV and 1 keV design are limited to a 10 kV voltage; therefore Z focusing must be accomplished using other methods. Focusing along the Z direction can also be accomplished by changing the focal length of the lens. Usually, Z focusing is more effective as the focal plane is moved away from the lens assembly. Unfortunately, the 400 eV and 1 keV designs are limited in this regard as well. High initial energy photoelectrons are focused to higher radial positions on the detector than lower initial energy photoelectrons (see fig. 6b). The proximity of the detector to the lens assembly therefore affects the maximum photoelectron energy it can distinguish. One additional way a lens may be focused in the Z direction is by changing $X_v$. For a given focal length and voltage magnitude, $X_v$ can be changed to optimally Z focus the lens. The 400 eV design requires a relatively short focal length compared to the design in [1], therefore the Z focusing capability of this lens is somewhat limited for low lens voltage magnitudes.

A Z focusing optimization algorithm was written by Matthias Keubel [1]. The optimization routine works by measuring photoelectron time of flight along various positions on the spectrometer axis, assuming zero initial photoelectron velocity along this direction. By inputting time of flight positions around the desired interaction region, it is possible to get a measure of the consistency in time of flight between parts of the interaction region separated along the spectrometer axis. A lens is more or less in focus along the Z direction if the spread in time of flight in the interaction region along the spectrometer axis is minimized. An optimized Z focusing plot is shown in fig. 8 for a modified version of Matthias Keubel's lens design, where the distance from the extractor plate to the interaction region was 7 mm. In this plot, the distance from the ground plate to the detector was assumed to be 73 mm and a 10 kV bias was applied to

the repeller. The lens was optimally Z focused at $X_v$ = .6198. When the lens components are charged to high voltages (10 kV or higher), the differences in time of flight between parts of the interaction region in optimized and un-optimized lens designs becomes essentially negligible. Using the design from figure 5b with an optimal Z focus, the difference in time of flight between s0 = 7 mm and s0 = 7.5 mm is $\approx 1.889 \times 10^{-10}$ seconds, which increases by roughly a factor of 1.5 for an unfocused lens with $X_v$ = .82. The photoelectron times of flight are fractions of nanoseconds in either case, which is completely indistinguishable by the detector, which has a response time of roughly 100 nanoseconds.

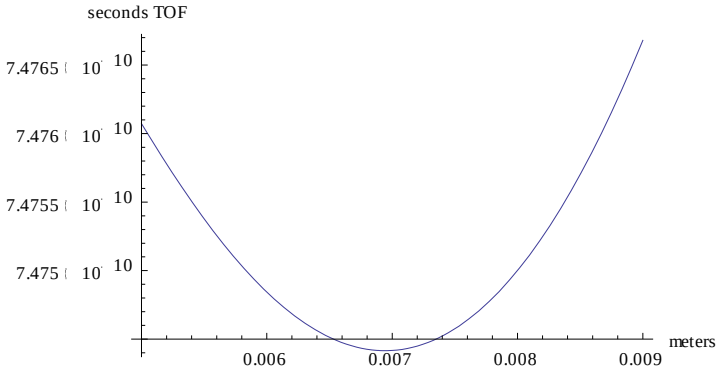


Figure 8: Photoelectron time of flight versus interaction region position measured from the extractor plate s0 (i.e. 6 mm is closer to the detector than 9 mm on the plot)

Achieving the maximum energy resolution of the lens by focusing the interaction region in the X and Y directions is a more difficult and necessary procedure compared to focusing along the spectrometer axis. The interaction region is essentially cigar shaped, with the long dimension along the propagation direction of the laser. Constricting the apparent size of the interaction region along this direction (X) is therefore more difficult. The focusing mechanism along the X and Y directions is also different than Z, which relies only on the value of $X_v$ and not the voltage magnitude of the lens components.

The master's thesis of Matthias Keubel [1] also features an optimization routine for focusing along the X and Y directions in the interaction region. The routine uses a Windows batch file program designed to communicate with Simion 7.0 iteratively. To run the program, a user first inputs a lens design in Simion with a fixed focal plane distance and lens plate geometry. The program then iteratively simulates a fixed number of photoelectron trajectories with a given spacing along the laser propagation direction. During each iteration the photoelectron energies and positions along the spectrometer axis are changed and $X_v$ is varied over a specified range to minimize the spot size of the photoelectrons on the detector. Minimizing the spot size on the detector also directly minimizes $\Delta E/E$ for a given radial position on the detector, as indicated by eqn 11. As the program runs, it records and stores information regarding the lens performance. In particular, it records the optimized spot size $\Delta r$ based on a

value of $X_v$ and the position r of the entire photoelectron group as it strikes the detector. This information in conjunction with the photoelectron energy values can be used to model the spectrometer function of the lens r(E) and the lens resolution capabilities.

Assuming that the lens voltage magnitude and geometry is sufficient for collecting photoelectrons on the detector surface, the X-Y focusing routine can be used to test lens designs for optimal resolution. During lens testing, the linearity of the spectrometer function of the lens design is tested with the energy resolution of the design $\Delta E/E$. A more linear spectrometer function indicates that the energy resolution equation given by eqn 11 is a more or less adequate approximation. There are many factors in the lens design that may affect the linearity of the spectrometer function or the resolution capability of the lens. Qualitatively, the position of the lens focal plane affects the resolution highly. As discussed previously, lenses with shorter focal plane positions (closer to the ground plate) generally have less resolution capability then lenses with longer focal plane positions. Another qualitative feature that affects the resolvability of VMI lenses is the image field curvature of the lens. Lenses with more or less curved equipotential lines near the interaction region have less or more resolvability because of this effect, where photoelectrons converge to a curved focal plane. Lenses with wide apertures tend to have more linear spectrometer functions because the photoelectron trajectories are less bent by the lens plates on their way to the detector.

**Results: Two Photoelectron Energy Scale Lens Design Models**

Using the optimization routine from the previous section, two separate VMI lens designs have been modeled. The first design has been constructed for resolving up to 400 eV photoelectrons with excellent resolution. The spectrometer function of this design is very nearly linear for all photoelectron energies. The second design is capable of fitting up to 1 keV photoelectrons onto a 75 mm detector with a very short focal plane position. The spectrometer function deviates from linearity somewhat; therefore the resolution measurements of the lens following eqn 11 may contain errors. There is additional resolution concerns involved with this lens design, however it is likely that its resolution will be high enough to distinguish 1 keV photoelectrons with a sufficient degree of accuracy for strong field experiments.

**I. 1-400 eV High Resolution Design**

The VMI low energy design will likely be used in lower wavelength strong-field experiments (0.8 – 2 μm) and attosecond experiments. It is designed for upper photoelectron energies of 400 eV, but achieves its best performance when resolving photoelectrons with 250 eV energies and below. This design has high resolution for all photoelectron energies within its range and a very strongly linear spectrometer function for photoelectrons with 80 eV energies and below. A 2-D diagram of this design in Simion is shown below in fig. 9. The resolution ability of this design is shown in figs. 10a and 10b. This figure shows how the lens may be tuned for maximum resolution of a specific photoelectron energy by changing $X_v$ to bring different

photoelectron energies into focus. The lens resolution and spectrometer function plots were obtained using the X-Y focusing program written by Matthias Keubel [1].

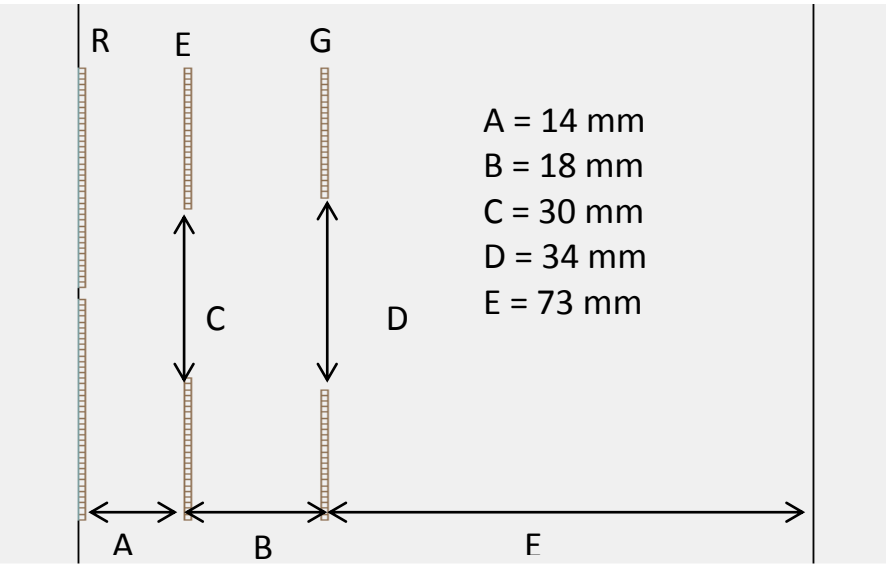


Figure 9: 2-D cross-section of 400 eV VMI lens design in the Simion interface. The repeller (R), extractor (E) and ground (G) plates are labeled as shown. The geometric values of the lens were optimized for the best possible lens resolution. The interaction region of the lens is located 7 mm in front of the extractor plate. The black line on the right of the figure represents the detector.

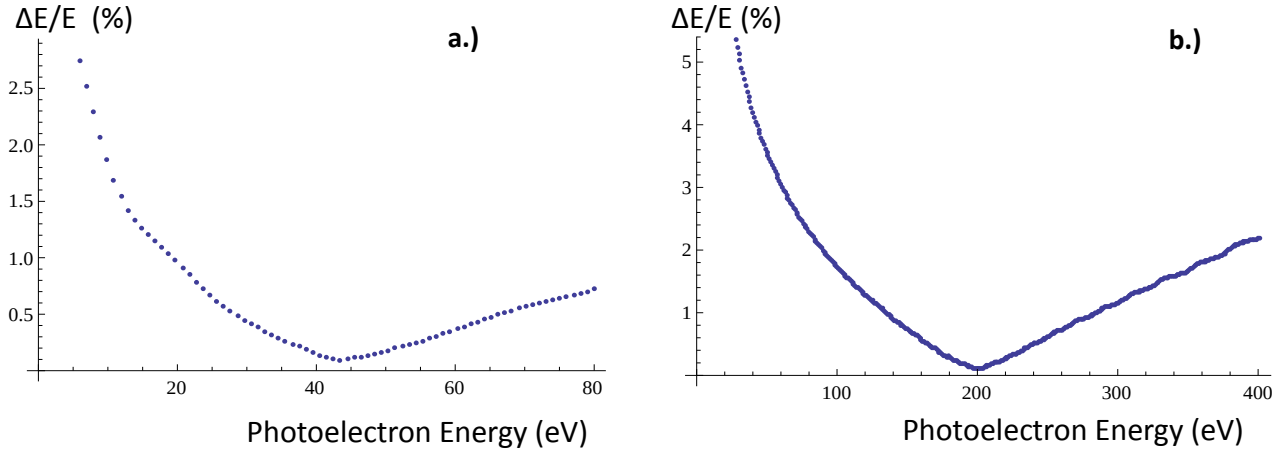


Figure 10: a.) Resolution versus photoelectron energy for photoelectron energies from 0-80 eV. The interaction region length is 1.0423 mm, using a 3.6 μm wavelength laser focused with an f/# = 4 lens. 5 photoelectrons were launched from equally spaced positions along the interaction region length. $X_v$ was set to 0.875 with a -10 kV repeller voltage. b.) Resolution versus photoelectron energy for photoelectrons energies from 10-401 eV (1-9 were omitted for graph scaling). Five photoelectrons were launched along a 1.0423 mminteraction region length. $X_v$ = 0.850.

The spectrometer function of the low energy lens is shown in figs. 11a and 11b. The data in these figures were collected by recording the detected positions of photoelectrons launched along the laser polarization direction. Figure 11a shows 400 recorded photoelectrons from 1-401 eV and fig. 11b shows 80 recorded photoelectrons from 1-81 eV. The radial distance on the detector was plotted as a function of the square root of energy and a least squares routine was performed to obtain a linear fit for the data. The square of the correlation coefficient for each linear fit was also calculated and was found to be 0.999606 for the 1-401 eV data set and 0.999992 for the 1-81 eV data set, indicating a strong linearity in each. Figure 11a shows that photoelectrons with energies near 400 eV begin to curve the spectrometer function, which moves the y-intercept of the linear fit line away from the origin to y = 0.5843, whereas the 80 eV linear fit passes very near the origin with a y-intercept of 0.0428. The real spectrometer function of the lens will necessarily pass through the origin as photoelectrons with zero energy will be found at r = 0. Using the 80 eV data least squares fit line as a linear fit to the 400 eV data produces a squared correlation coefficient of 0.9881. This value indicates strong linearity, but deviates from the 80 eV squared correlation coefficient by 1.19%.

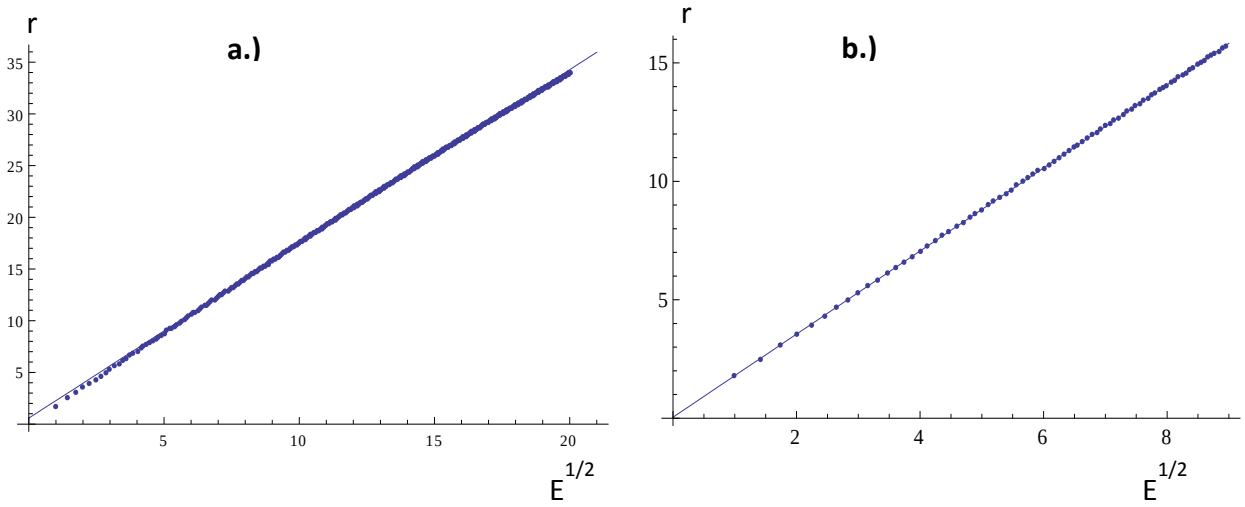


Figure 11: a.) Linear spectrometer function for 400 eV design showing entire energy range. Blue dots represent modeled data points while the blue line represents a linear least-squares fit. The linear least-squares line has been calculated to be $r(E^{1/2}) = 0.5843 + 1.684E^{1/2}$. The $r^2$ measurement for this fit was 0.999606. b.) Linear spectrometer function for 400 eV design showing least squares fit for photoelectron energies from 1-81 eV. The best fit for this line was calculated to be $r(E^{1/2}) = 0.04276 + 1.7537E^{1/2}$. The $r^2$ measurement for this fit was 0.999992.

## II. 1 keV Lens Design

As the photoelectron initial energy increases, so too must the aperture sizes of the lens to avoid photoelectron clipping on the lens apertures. The 400 eV design required applying this idea to previous VMI lens designs which eventually resulted in the relatively large lens apertures

shown in figure 9. To reiterate, the position of the detector must also be pushed inward, toward the repeller plate, as the photoelectron energy increases. The distance between the lens focal plane and ground plate was changed by 53 mm in the 400 eV design from Matthias Kuebel's 80 eV design [1] to accommodate higher energy photoelectron radial positions on the detector. To create a lens design capable of resolving up to 1 keV, this step had to be repeated on the 400 eV lens design, where the distance from the ground plate to the detector is only 48 mm. Shown in fig. 12 is a proposed lens design that can resolve up to 1 keV photoelectrons. Some of the consequences of applying an extremely short lens focal length have been discussed previously, such as an expected decrease in the lens resolution. The large lens apertures also decrease the overall resolution of the lens on lower energy photoelectrons because the lens plates have less influence on the photoelectron trajectories. One positive consequence of this extreme lens design is the spectrometer function for low energy photoelectrons is very linear because of the lower influence the lens plates have on bending the photoelectron trajectories. This means that photoelectron positions on the detector and resolution calculations will be very accurate for lower energy photoelectrons. The least squares fit of the spectrometer function for 1-80 eV photoelectrons is given by eqn. 12, with an $r^2$ value of 0.999996. A plot of the 80 eV spectrometer function with least squares fit is shown in fig.13a. The spectrometer function of the entire energy distribution up to 1 keV has a much stronger deviation from linearity as shown in

$$r\left(E^{\frac{1}{2}}\right) = 0.0211 + 1.2945E^{1/2} \tag{12}$$

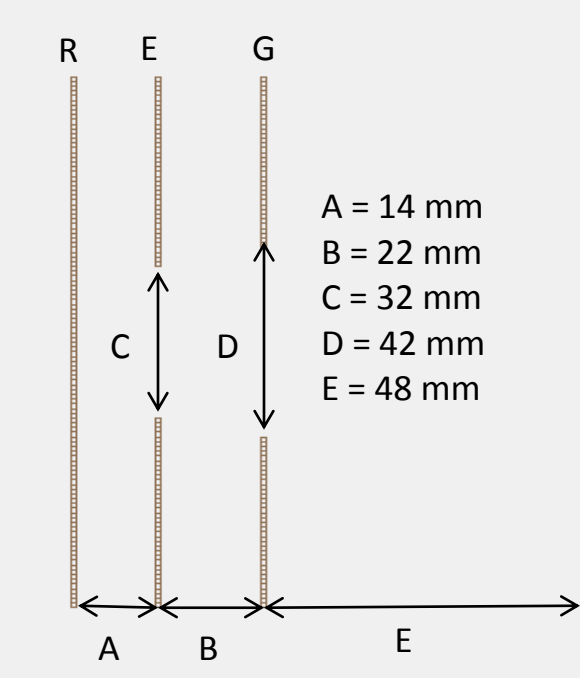


Figure 12: 1 keV lens design in the Simion interface. Compared to fig. 9, the values of B, C, D and E have changed. The edge of the figure indicates the detector position.

fig. 13b. The spectrometer function has a y-intercept of 1.5769 and a squared correlation coefficient of 0.9970. Using the 80 eV spectrometer function obtained for this lens design as a linear fit for the 1 keV data gives a squared correlation coefficient of 0.9445, which deviates

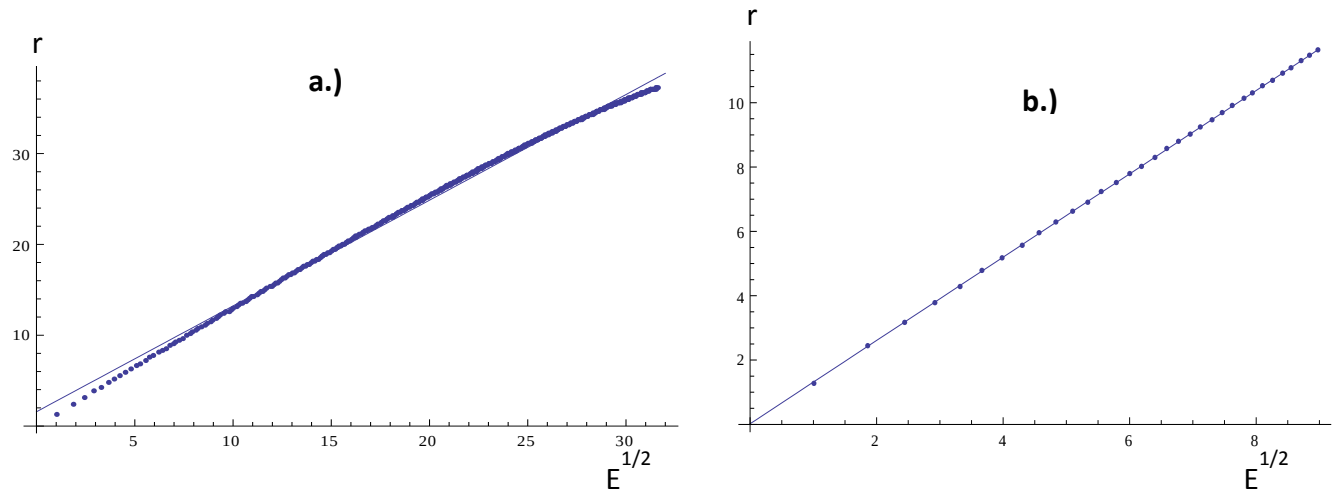


Figure 13: a.) Linear spectrometer function for 1 keV design showing entire energy range. Blue dots represent modeled data points while the blue line represents a linear least-squares fit A linear least-squares line has been calculated to be $r(E^{1/2}) = 1.5769 + 1.1643E^{1/2}$. The $r^2$ measurement for this fit was 0.997025. b.) Linear spectrometer function for 400 eV design showing least squares fit for photoelectron energies from 1-81 eV. The best fit for this line was calculated to be $r(E^{1/2}) = 0.0211 + 1.2945E^{1/2}$. The $r^2$ measurement for this fit was 0.999996.

from the 80 eV value by 5.55%. The lower energy least squares fit line in fig 13b is likely a very good estimate for the actual spectrometer function due to its high linearity and low y-intercept value. It is therefore worthwhile to compare the deviation of the high energy modeled data in fig. 11a from the linear fit from the linear fit in fig. 11b. Figure 14 shows the deviation of the linear fit line for the entire 1 keV data set from the fit line for photoelectrons up to 80 eV within this data set. The maximum deviation was found to be 9.14% at 1 keV. Although this error is significant, it will likely not affect the experimental performance of the lens. The resolution of the lens may be tuned to $\Delta E/E = 2.74\%$ at 1 keV at best. If the 9.14% error is accounted for in the radial position of the 1 keV photoelectron, $\Delta E/E$ increases to 3.01%, which is likely an acceptable error measurement.

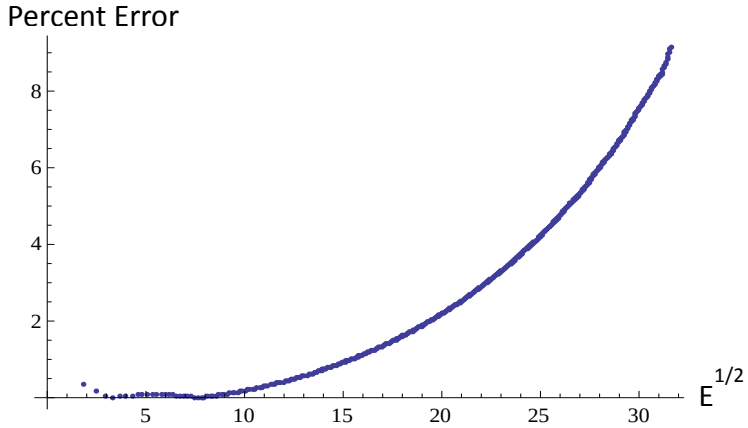


Figure 14: Percent error as a function of photoelectron energy $E^{1/2}$ for the 1 keV lens design. The percent error measures the amount the 1 keV data points deviate from the linear least squares fit of the 1-80 eV photoelectrons in this data set.

The resolution of the lens is calculated without error bars in figs 15a. and 15 b. The lens is tuned to resolve higher and lower photoelectron energies in each figure and surprisingly outperforms the 400 eV lens at low energy. As expected, the resolution of the lens becomes poorer than the 400 eV design when tuned to higher energies as in fig. 15 b.

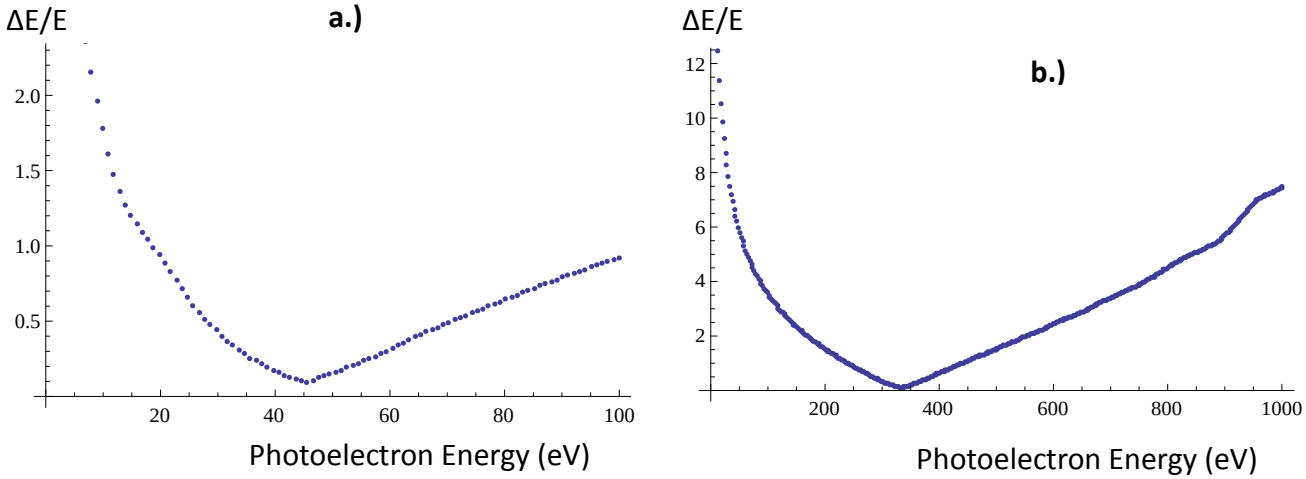


Figure 15: a.) Resolution versus photoelectron energy for photoelectron energies from 0-80 eV. The interaction region length is 1.0423 mm, using a 3.6 μm wavelength laser focused with an f/# = 4 lens. 5 photoelectrons were launched from equally spaced positions along the interaction region length. $X_v$ was set to 0.920 with a -10 kV repeller voltage. b.) Resolution versus photoelectron energy for photoelectrons energies from 10-1001 eV (1-9 were omitted for graph scaling). Five photoelectrons were launched along a 1.0423 mminteraction region length. $X_v = 0.880$.

Aside from the non-linear shape of the spectrometer function, other issues may exist that affect the performance of the 1 keV design. One issue in particular is an aberration effect of the lens when resolving photoelectron trajectories launched with large θ angles. This effect is shown graphically in figure 16. As was shown previously, photoelectrons with different launch angles θ should converge to the same place on the detector for a properly focused lens. This is true only if the photoelectron energy E >> $qV_R$. As the photoelectron energy increases, this condition becomes less and less valid, especially for large elevation angles. In figure 16, photoelectron trajectories with lower initial elevation angles θ converge to higher points on the detector, and it can be seen that these trajectories have a smaller spot size than photoelectrons launched with large angles θ. This is essentially because as the photoelectron energy increases to a comparable level with the lens energy, photoelectron flight paths change significantly with increased θ.

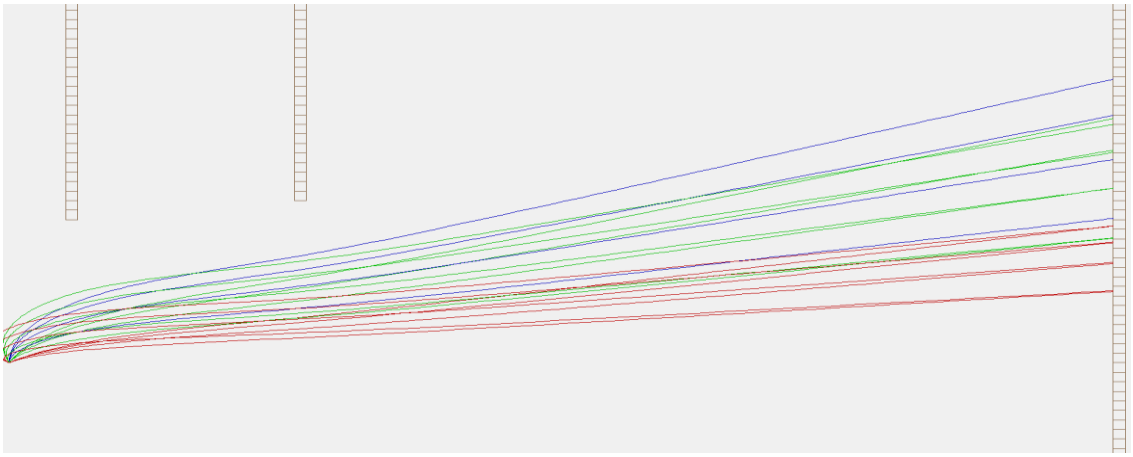

Figure 16: 200 eV photoelectrons launched with $V_R$ = -5000 from different elevation angles in the Simion interface. The range of launch angles extends from θ = -60 to θ = 60. At higher launch angles, the photoelectron spot sizes are noticeably larger on the detector.

Because of the large detector size and small interaction region length, it is possible that the 1 keV design will be very successful experimentally. It is possible to achieve high resolution with this design at all photoelectron energy levels with acceptable errors in the resolution calculations. It is also likely that there are several sources of error that will become significant, such as the aberrations shown in figure 16, which may limit the resolving power of the lens. The lens design will probably be constructed and tested in an experimental setting involving 3.6 μm strong field photoionization experiments.

**Conclusion and Project Outlook**

Because the design of the electrostatic lens component of the VMI essentially determines how the VMI will perform, this text has been dedicated to the modeling aspects of this component. Aside from modeling the electrostatic lens in the VMI, a great deal of time on the project has been spent on the actual assembly of the device within the vacuum chamber. The design shown in fig. 5 is a model showing how the VMI components, the lens and the detector, will fit together. A great deal of the project work was devoted to the design of individual parts that went into this 3-D rendering, such as the copper stand that the detector will be attached to in fig. 4 or the 8'' flange design. The actual construction process of the VMI will take place during the summer of 2011, while work will continue on the lens design as well. The device is meant to be customizable, so the assembly shown in fig. 4 can be easily moved in and out of the vacuum chamber as individual parts are changed. The focal length of the lens may be decreased in this design, but has a maximum length given by fig. 9. The lens plates will be constructed out of a sheet of molybdenum alloy, which is large enough such that several lens designs may be cut out of a single sheet. When the device is operational, several lens designs may be tested for each experiment to compare the lens performance to modeling.

Using the lens design and modeling methods from Matthias Keubel's thesis as a template, two lens designs have been constructed and modeled. The first design is capable of resolving up to 400 eV photoelectrons from strong field experiments with a performance emphasis on 1-100 eV photoelectrons. This design has shown very good resolution capabilities at lower energies and a strongly linear spectrometer function, indicating low error in the lens resolution measurements. A second prototype design has been constructed for resolving photoelectrons with energies up to 1 keV. Surprisingly, this design model also has very good performance for lower energy (1-100 eV) photoelectrons, with good resolution up to 1 keV. The spectrometer function for all energies deviates from linearity significantly, indicating possible errors in the lens resolution. There may be additional resolution concerns that were not found during the modeling procedure. Both of these designs will likely be tested in the constructed VMI apparatus and their overall performance will be measured in photoelectron experiments.

**Works Cited**

[1] M. Kuebel, *Photoionization with Intense Laser Fields: Imaging and High Frequency Limit*, Diplomarbeit. Friedrich-Schiller-Universit¨at Jena, (2010).

[2] M. Lewistein et al, *Theory of High Harmonic Generation by Low-Frequency Fields*, Phys. Rev. A. **49:3**, 2117-2132 (1994).

[3] P. Agostini and L.F. DiMauro, *The Physics of Attosecond Light Pulses*, Rep. Prog. Phys. **67**, 813-855 (2004).

[4] L.F. DiMauro and K.C. Kulander, *Strong Field Atomic Physics*, SIF Bologna Conference Proceedings. **88**, (2004).

[5] H. L. Offerhaus et al, *A Magnifying Lens for Velocity Map Imaging of Electrons*, Rev. Sci. Instrum. **72**, 3245-3248 (2001).

[6] A. T. J. B. Eppink and D. H. Parker, *Velocity Map Imaging of Ions and Electrons Using Electrostatic Lenses: Application in Photoelectron and Photofragment Imaging of Molecular Oxygen*, Rev. Sci. Instrum. **68**, 3477 (1997).

[7] C.A. Bennett, *Principles of Physical Optics*, 1st ed. John Wiley & Sons, New York (2008).

[8] P. Colosimo et al, *Scaling Strong-Field Interactions Toward the Classical Limit*, Nature Physics. **4**, 386-389 (2008).

[9] V. Dribinski et al, *The Reconstruction of Abel-Transformable Images*, Rev. Sci. Instrum. **73**, 2634-2642 (2002).

[10] M. J. J. Vrakking, *An Iterative Procedure for the Inversion of Two-Dimensional Ion/Photoelectron Imaging Experiments*, Rev. Sci. Instrum. **72**, 4084-4089 (2001).